Journal of Nuclear Materials 466 (2015) 606–614

Contents lists available at ScienceDirect

Journal of Nuclear Materials

journal homepage: www.elsevier.com/locate/jnucmat

In situ ion irradiation of zirconium carbide

Christopher J. Ulmer [a, *], Arthur T. Motta [a], Mark A. Kirk [b]

[a] Department of Mechanical and Nuclear Engineering, The Pennsylvania State University, University Park, 16802 PA, USA
[b] Nuclear Engineering Division, Argonne National Laboratory, Argonne, IL 60439, USA

HIGHLIGHTS

- $ZrC_{0.8}$ and $ZrC_{0.9}$ were irradiated *in situ* at the IVEM using 1 MeV Kr ions at temperatures ranging from 20 to 1073 K.
- The irradiated microstructure coarsened during irradiation at higher temperatures.
- The dose evolution of defect size and density was measured at several irradiation temperatures.
- The irradiated microstructure did not depend strongly on stoichiometry.

ARTICLE INFO

Article history:
Received 4 May 2015
Received in revised form
4 August 2015
Accepted 5 August 2015
Available online 10 August 2015

Keywords:
Nuclear materials
Zirconium carbide
Ion irradiation
Defects

ABSTRACT

Zirconium carbide (ZrC) is a candidate material for use in one of the layers of TRISO coated fuel particles to be used in the Generation IV high-temperature, gas-cooled reactor, and thus it is necessary to study the effects of radiation damage on its structure. The microstructural evolution of ZrC_x under irradiation was studied *in situ* using the Intermediate Voltage Electron Microscope (IVEM) at Argonne National Laboratory. Samples of nominal stoichiometries $ZrC_{0.8}$ and $ZrC_{0.9}$ were irradiated *in situ* using 1 MeV Kr^{2+} ions at various irradiation temperatures (T = 20 K–1073 K). *In situ* experiments made it possible to continuously follow the evolution of the microstructure during irradiation using diffraction contrast imaging. Images and diffraction patterns were systematically recorded at selected dose points. After a threshold dose during irradiations conducted at room temperature and below, black-dot defects were observed which accumulated until saturation. Once created, the defect clusters did not move or get destroyed during irradiation so that at the final dose the low temperature microstructure consisted only of a saturation density of small defect clusters. No long-range migration of the visible defects or dynamic defect creation and elimination were observed during irradiation, but some coarsening of the microstructure with the formation of dislocation loops was observed at higher temperatures. The irradiated microstructure was found to be only weakly dependent on the stoichiometry.

1. Introduction

Generation IV nuclear reactors are conceived to provide improvements in sustainability, safety, reliability, economics and proliferation resistance over current reactors [1]. One such reactor concept is the high-temperature gas-cooled reactor or, more specifically, the very-high-temperature reactor (VHTR). The VHTR concept utilizes helium coolant with high outlet temperature to improve thermal energy conversion efficiency. The tristructural isotropic (TRISO) fuel, a type of coated fuel particle, is the basic fuel form of the VHTR [2].

The TRISO fuel particle design includes a load-bearing SiC layer which serves as a barrier to fission gas release. However, there are some limitations for the use of SiC in the TRISO fuel design. SiC may be thermally unstable in the temperature range that could be reached during accident conditions so that it could undergo a β-SiC to α-SiC transformation, resulting in failure of the layer and the consequent release of fission products [3]. Additionally, the SiC layer is susceptible to attack by palladium (one of the fission products), which can corrode the inner surface of the SiC layer and potentially compromise the retention of fission products [4]. Because of these limitations, a variation on the standard TRISO fuel design was proposed in which a zirconium carbide (ZrC) layer would be used in place of the SiC layer [5].

Because of its intended use as the load-bearing layer in TRISO

* Corresponding author.
E-mail address: cju5002@psu.edu (C.J. Ulmer).

http://dx.doi.org/10.1016/j.jnucmat.2015.08.009
0022-3115/

fuel for a VHTR, the response of ZrC to radiation damage must be understood. A number of investigations into the microstructural changes of ZrC under irradiation have been carried out in the past. Gan et al. [6] conducted *in situ* irradiations of $ZrC_{1.01}$ up to 10 and 30 dpa at room temperature and 10 and 70 dpa at 800 °C using the Intermediate Voltage Electron Microscope (IVEM). A high density of black-dot defects was found at room temperature, and dislocation segments were observed at 800 °C. Bulk ion irradiations of ZrC were performed by Yang et al. [7] using 2.6 MeV protons to 0.7 and 1.5 dpa at 800 °C who observed the formation of Frank loops, and by Gosset et al. [8] using 4 MeV Au ions at room temperature who found a high density of small defects which evolved into a dense dislocation network as the dose increased. Neutron irradiations were carried out by Snead et al. [9] using the High Flux Isotope Reactor to fast neutron fluences of $0.8-9.38 \times 10^{25}$ neutrons/(m^2s) at temperatures ranging from 635 to 1496 °C. The neutron irradiations resulted in the formation of dislocation loops which transitioned in nature from Frank to prismatic loops at higher temperatures. Some investigation into the effects of ZrC_x stoichiometry on the irradiation response have been conducted using bulk proton irradiations at 800 °C to 1–3 dpa [10] and 1125 °C to 2 dpa [11]. However, there has been no systematic investigation into the effect of temperature on the accumulation of radiation damage in ZrC, and no irradiations have been performed at cryogenic temperatures where athermal reactions can be studied. Additionally, understanding of the effects of ZrC stoichiometry on radiation damage is limited with respect to irradiation temperature and dose.

This research is aimed at reaching a greater understanding of the fundamental irradiation response of ZrC. To further this goal, irradiations were carried out on ZrC_x using 1 MeV Kr^{2+} ions while the evolution of the microstructure was simultaneously investigated using transmission electron microscopy (TEM). A range of irradiation temperatures were used, from cryogenic temperatures at which defects should have minimal mobility to high temperatures where the defects can move to form larger clusters. The irradiation temperature was systematically varied to determine its detailed effect on defect kinetics. Samples of two different stoichiometries were prepared and irradiated to determine the effect of stoichiometry on microstructural evolution under irradiation. Because the experiments were conducted *in situ*, the microstructure could be continuously followed, allowing for the direct observation of defect accumulation mechanisms as they occurred and more detailed inferences on the mechanisms. Finally, the effects of pre-existing microstructure, such as dislocations, and of the sample surface on damage accumulation were investigated.

2. Experiment

2.1. ZrC samples

Rods of ZrC_x with nominal stoichiometries of x = (0.8,0.9) were purchased from Applied Physics Technologies, Inc. Polycrystalline ZrC_x was produced by a modified arc, floating zone refining process [12]. The compositions were verified by the ATI Wah Chang Analytical Laboratory using a combustion-IR method which, for the two target stoichiometries, measured stoichiometries of x = (0.794, 0.890) respectively.

Table 1
Parameters for electropolishing ZrC_x, x = (0.8,0.9).

Apparatus	Struers Tenupol-5
Electrolyte solution	7.5% perchloric acid 92.5% methanol
Electrolyte temperature	243 K
Voltage	25 V
Light stop value	60
Pump flow rate	26

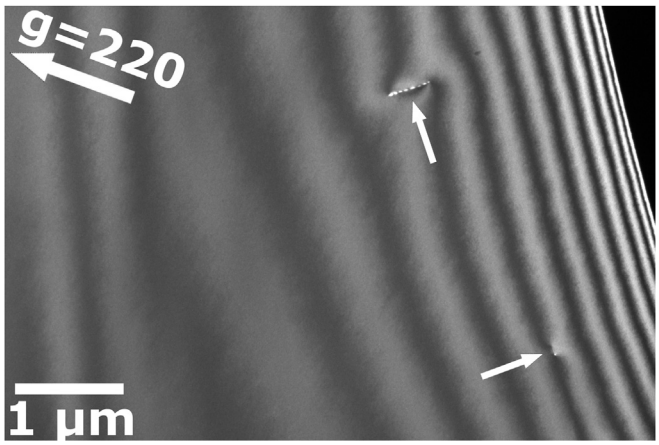

Fig. 1. Dark-field TEM micrograph (g,3g) of the unirradiated microstructure of $ZrC_{0.9}$. Two dislocations present before irradiation are indicated by arrows.

The ZrC_x was received as rods with 3 mm diameter and approximately 3 cm length. Samples were prepared by first sectioning the rod into disks using a low-speed saw with metal-bonded diamond wafering blade. The disks were then thinned to approximately 200 μm thickness using successive grinding and polishing steps with 400, 600 and 800 grit SiC abrasive disks. Finally, the samples were prepared for transmission electron microscope (TEM) examination by electrolytic polishing using a Struers TenuPol-5. The electropolishing settings are provided in Table 1. The samples were removed and rinsed in methanol and ethanol immediately after electropolishing and stored in ethanol until their use.

This sample preparation method produced samples with a "clean" microstructure, featuring a single ZrC_x phase with large grains and a low dislocation density before irradiation. Typically only a single grain was visible in the electron-transparent region of the TEM samples. Fig. 1 shows a low magnification dark-field TEM image taken from $ZrC_{0.9}$ before irradiation which demonstrates the features described above. Because the microstructure was relatively free of features, a dislocation was typically chosen as a marker to be followed throughout an experiment.

2.2. IVEM irradiations

Irradiation experiments were conducted at the Intermediate Voltage Electron Microscope (IVEM) facility at Argonne National Laboratory [13]. The IVEM consists of a Hitachi H-9000NAR transmission electron microscope (TEM) interfaced with an ion accelerator to allow for concurrent ion irradiation and TEM examination of a sample. This capability makes it possible to continuously follow the evolution of the microstructure due to irradiation in real time. Dynamic processes such as defect creation, annihilation and interaction can be observed, and the IVEM is equipped to record video of the microstructure evolution during irradiation for later analysis.

The irradiations in this study were performed using 1 MeV Kr^{2+} ions at a flux of 6.25×10^{15} ions/(m^2 s). 1 MeV Kr ions were chosen because a high dose rate can be achieved, the damage profile does not vary greatly in a TEM thin foil and the majority of ions pass completely through the thin foil. The equivalent dose in displacements per atom (dpa) was calculated using the Stopping and Range

Table 2
Input parameters for SRIM simulation.

Calculation type	Full cascade
Ion species	Krypton
Ion energy	1000 keV
Target width	100 nm
Target density	6.5 g/cm^3
Target composition	$ZrC_{0.9}$
Displacement energy	Zr = 37 eV [28]
	C = 16 eV [28]
Number of ions	10000

Table 3
List of experimental conditions in this study.

Material	T [K]	Max. Dose [dpa]
$ZrC_{0.9}$	20	6.4
	50	12.8
	300	6.4
	473	6.4
	673	3.9
	873	6.4
	973	6.4
	1073	12.8
$ZrC_{0.8}$	50	6.4
	300	6.4
	473	6.4
	673	6.4
	873	6.4
	973	6.4
	1073	6.4

of Ions in Matter (SRIM) program [14]. The input parameters used for the SRIM calculation are provided in Table 2. While the "Ion Distribution and Quick Calculation of Damage" option has been found to be more accurate in some cases (see Ref. [15]), A simulation involving 10,000 ions resulted in an average of 1872 ± 37 displacements per ion within the thin foil, assumed to be 100 nm thick.[1] This is equivalent to a dose rate of 1.6×10^{-3} dpa/s when averaged over the whole sample. For the purposes of reporting the dose in this study, 1 dpa is equivalent to a measured ion fluence of 3.9×10^{18} ions/m^2. By assuming surface binding energies equal to one-half the displacement energies, SRIM calculates a sputtering yield of 1.642 atoms/ion, or an equivalent removal rate of approximately 8.8×10^{-2} nm/dpa. Even at the maximum dose of 12.8 dpa, only 1.1 nm of material is removed from the nominally 100 nm thick foil.

Irradiations were conducted over a wide range of temperatures, ranging from 20 K to 1073 K. The full range of irradiation conditions is listed in Table 3. During the experiments, samples were heated or cooled to the desired temperature and then pre-irradiation images were acquired. Temperatures below room temperature were achieved using a double-tilt, liquid helium cooled cryo-holder. At room temperature and above, a double-tilt heating holder was used. Samples were then irradiated while recording video. At selected dose points, the irradiation was stopped to allow the operator to realign microscope settings and acquire images and diffraction patterns to document the evolution of the microstructure at the selected points before continuing the experiment. This method was repeated until the final dose point, typically 6.4 dpa, was achieved. Irradiation induced defects were imaged using both bright-field and dark-field diffraction contrast imaging.

The sample temperature is measured by a thermocouple attached to the furnace cup. An estimate for the temperature difference between the edge of the sample where it is in contact with the furnace cup and the center where the irradiation was conducted was made because the sample temperature was not directly measured at the area observed using TEM. By assuming a 500 nm thick ZrC disk in which a 1.5 mm diameter 1 MeV Kr ion beam deposited all of its energy as heat evenly throughout the samples thickness, the center of the sample was calculated to have a temperature approximately 30 K greater than its edge if only radial heat conduction is considered. The exact value would depend on the sample geometry and the sample thermal conductivity which was nominally chosen as 20 W/mK. Considering that most of the sample is thicker than 500 nm, this should serve as an upper estimate of the error in temperature measurement. In contrast to the electron beam well-spread over the sample, turning the ion beam on and off results in no change to the temperature measured in the furnace cup, which could indicate that the ion beam produces negligible sample temperature increase.

Defect density and size were determined by manually counting and measuring defects using the ImageJ [16] image manipulation program. This analysis was performed for dark-field images acquired using a g = 220 type diffraction vector with a semi-weak (**g**,3**g**) condition. Defect diameters were measured along the longest axis of a given defect. The local sample thickness was determined by means of thickness fringes in two-beam bright-field images. The extinction distance was calculated using

$$\xi_g = \frac{\pi V_c \cos\theta_B}{\lambda F_g} \tag{1}$$

where V_c is the volume of the unit cell, θ_B is the Bragg angle, λ is the electron wavelength, and F_g is the structure factor [17]. The structure factor for ZrC is given by

$$F_g = \begin{cases} 4(f_{Zr} + f_C) & \text{if h, k, and l are all even} \\ 4(f_{Zr} - f_C) & \text{if h, k, and l are all odd} \\ 0 & \text{otherwise} \end{cases} \tag{2}$$

where f_{Zr} and f_C are the atomic scattering amplitudes for Zr and C, and h, k and l are the indices of atomic planes. Using the atomic scattering amplitudes in Ref. [18], the extinction distance is calculated to be 54 nm for g = 220 in ZrC with a lattice parameter $a_0 = 0.47$ nm while operating a TEM at 200 keV. The extinction distance was also measured by convergent beam electron diffraction (CBED) as outlined by Kelly et al. [19]. Operating the TEM at 200 keV, the extinction distance was found to be 56.6 nm, approximately 5% larger than the calculated value. The calculated extinction distance was used when determining sample thickness.

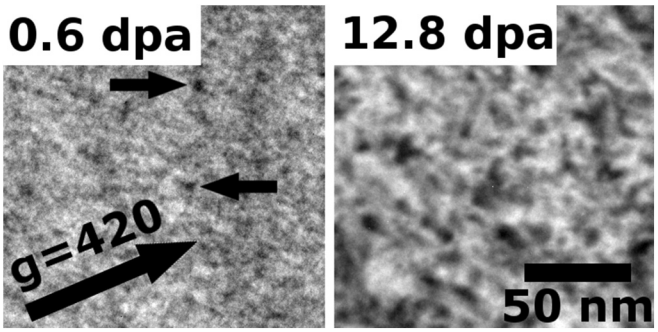

Fig. 2. Bright-field TEM micrographs with g = 420 showing the dose evolution of irradiated microstructure of $ZrC_{0.9}$ at 50 K. Doses of 0.6 and 12.8 dpa are shown. Small arrows point to examples of defects formed at 0.6 dpa.

[1] The damage rate is 1380 ± 25 displacements per ion when using the "Ion Distribution and Quick Calculation of Damage" option in SRIM.

3. Results

The experimental results are discussed in this section and are organized by irradiation temperature. Additional observations are then discussed separately.

3.1. Dose evolution of irradiated microstructure

During irradiation at a temperature of 50 K, no damage was seen up to a dose of 0.6 dpa when small, black-dot defects (white spots in dark-field) started to appear. The density of this black-dot damage increased swiftly with dose up to 2.6–3.9 dpa, at which point the rate of damage accumulation appeared to decrease. Representative images of the damage progression are shown in Fig. 2. The initial defects seen at 0.6 dpa are arrowed. The defect density does not appreciably change between 6.4 and 12.8 dpa. The defects, once created, were stable (no defects disappeared once created) and immobile during irradiation, such that the defect density simply increased to saturation. This is in contrast to other experiments, such as the *in situ* irradiation of alloy NF616, in which a dynamic equilibrium was observed with defects appearing and disappearing when the ion beam was on [20].

Of interest to the performance of this compound under irradiation is its susceptibility to irradiation induced amorphization. Previous studies had shown that amorhpization did not occur in ZrC at temperatures down to room temperature. Because amorphization is most favored at low temperature [21], we investigated sample behavior at cryogenic temperatures. No amorphization was observed, even after irradiating to 12.8 dpa at 50 K and to 6.4 dpa at 20 K. This indicates a high resistance to amorphization, which agrees with theoretical considerations as outlined by Zheng et al., including high antisite defect energies, over-constrained topology and high concentration of carbon vacancies [22].

Fig. 3 shows images acquired while irradiating $ZrC_{0.9}$ at 673 K, in which damage appeared by 0.4 dpa as black-dot defects. At this irradiation temperature the defect clusters increased in size and density with increasing dose. Individual defects could be followed throughout the irradiation and all defects observed were motionless whether during irradiation or during post irradiation annealing. By 3.9 dpa, small dislocation loops were visible that showed "coffee bean" contrast, i.e. with double-arc contrast (see defects indicated by black arrows in Fig. 6). The increase in defect size during irradiation at 673 K, which did not occur during irradiation at 50 K, likely indicates that sub-visible defects or defect clusters are thermally mobile at this temperature.

The highest irradiation temperature in this study was 1073 K. The evolution of the irradiated microstructure in $ZrC_{0.9}$ with dose at 1073 K is shown in Fig. 4. When irradiating at 1073 K, the threshold to observe radiation damage was also 0.4 dpa, showing up first as black-dot defects. Both the defect density and the defect size increased with dose between 0.4 and 1.3 dpa, at which point a few small dislocation loops were present. As the dose increased further to 2.6 dpa, coalescence of smaller defects was observed as they formed dislocation loops with diameters up to approximately 30 nm (as shown in Fig. 5). Images acquired near a ⟨220⟩ zone axis show edge on loops consistent with {111} and {220} habit planes. These habit planes could indicate the presence of Frank loops and prismatic loops, both observed to result from neutron irradiation [9]. The microstructure continued to visibly coarsen until 5.1–7.7 dpa, beyond which dose little change in the microstructure was observed. At the end of the irradiation the microstructure showed a tangled dislocation structure, which could result from the projected image of overlapping dislocation loops.

During irradiation at 1073 K, while no apparent long-range motion of visible defects was observed, interaction of closely spaced defects, possibly by defect strain-field interactions, was observed after high defect densities were achieved, i.e. greater than 1.3 dpa. A series of images captured from the video recorded between 1.3 and 2.6 dpa is shown in Fig. 5. These images, showing dose steps of 0.4 dpa, are centered on an area which initially contained only black-dot damage or small dislocation loops of similar size at 1.3 dpa. A larger dislocation loop with non-circular shape began to form by 1.8 dpa. The loop then grew and became more circular as the dose was increased to 2.6 dpa. Based on the video, it is likely that the loop formed and grew by coalescence of smaller defects. Because this defect coalescence and coarsening is only observed at higher temperatures, it likely results from thermally activated motion of defect clusters.

It is interesting to directly compare the microstructures resulting from irradiation to 6.4 dpa at different temperatures, as shown in Fig. 6. During irradiation at 300 K, the microstructure was dominated by black-dot defects. In contrast, the small loops showing double-arc contrast also seen at 673 K were observed at 473 K. At higher irradiation temperatures, defect size increased further, such that at 873 K larger loops appeared, both with and without double-arc contrast. The microstructure coarsened further during irradiations conducted at 973 K and at 1073 K. At these irradiation temperatures the microstructure consisted of dislocation loops and tangled dislocation segments, which may result from the projection of overlapping dislocation loops visualized through the foil thickness. To summarize, higher irradiation temperatures resulted in larger defects with coarser microstructure, likely as a result of increased defect mobility.

3.2. Mean defect diameter and density

Fig. 7 shows the mean defect diameter measured as a function of dose for three different temperatures.[2] The series of measurements at each temperature were made from three single experiments. In general, defects were larger at higher irradiation temperatures. At 673 K, defect diameters were 2 nm when they initially formed at 0.4 dpa, increasing to approximately 4 nm at 3.9 dpa. At 873 K, defects were somewhat larger and first appeared with mean diameter around 2.5 nm, increasing to 5–6 nm after 3.9 dpa. The initial defects formed during irradiation at 1073 K had even larger diameters – around 4 nm, increasing to 8 nm by 3.9 dpa.

Fig. 8 shows the evolution of the defect density with irradiation dose for the same three temperatures. The measured defect densities were on the order of 10^{22} m^{-3} for the most part. Note that in each case the foil thickness was measured to turn an areal density

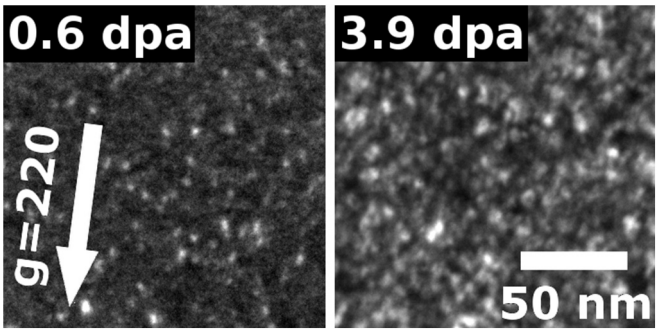

Fig. 3. Dark-field TEM micrographs imaged with g = 220 (g,3g) showing the dose evolution of the irradiated microstructure of $ZrC_{0.9}$ at 673 K up to 3.9 dpa.

[2] When "defect size" or "defect diameter" is referenced, it refers to a measurement of the contrast produced by the defect while using a given imaging condition.

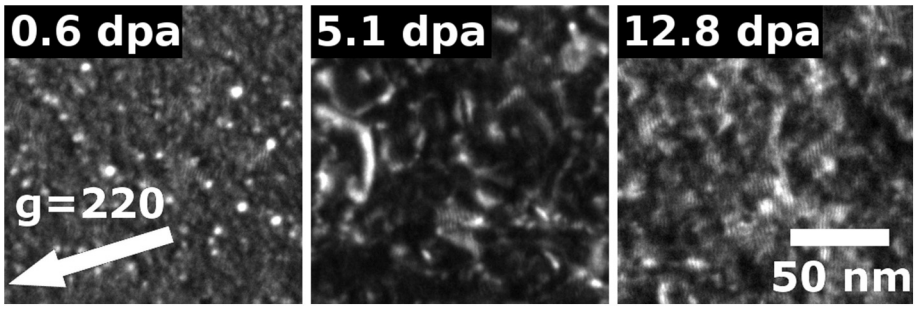

Fig. 4. Dark-field TEM micrographs imaged with g = 220 (g,3g) showing the dose evolution of irradiated microstructure of $ZrC_{0.9}$ at 1073 K. Coalescence of defects results in a coarse microstructure at this temperature.

into a volumetric density. At all temperatures, defect densities increased with dose up to 1.3 dpa. At 673 and 873 K, the defect density continued to increased up to 3.9 dpa, albeit at a lower rate than seen up to 1.3 dpa, likely because defect density saturation is being approached. At 1073 K, the defect density stopped increasing after 1.3 dpa and even decreased slightly when the dose increased to 2.6 dpa and 3.9 dpa, likely due to defect cluster coalescence resulting in a smaller number of larger defects. In general in this temperature range, defect density decreased with increasing irradiation temperature.

3.3. Thickness dependence of irradiated microstructure

During *in situ* irradiation of a thin foil, it is necessary to consider the effect of the thin foil surfaces on the microstructure evolution since these can act as sinks for point defects [24,23]. Clearly their effect will be most pronounced in the temperature region where the defect clusters are mobile and can interact with the foil surface. To assess this effect, the microstructure formed at different foil thicknesses was studied by examining a wedge-shaped foil of $ZrC_{0.9}$ irradiated at 1073 K at various distances from the foil edge. The irradiated microstructure was observed to strongly depend on the foil thickness. Fig. 9 shows a bright-field micrograph acquired near the sample edge after irradiation to 5.1 dpa at 1073 K. A defect-denuded zone is observed at the edge of the sample, the thinnest part of the sample. With increasing thickness, first black-dot defects are seen and then larger, resolvable dislocation loops are observed. A similar dependence of irradiated microstructure on foil thickness was also observed during irradiations performed at 973 K and 873 K. This variation of the irradiated microstructure likely resulted from the loss of defects at the foil surface. In the thinner region of the foil, the depth from where defects can migrate to the surface can be greater than the foil thickness, in which case no defect accumulation can occur. In the thicker region of the foil, defect motion can result in the formation of larger defects, such that the defect size increases with foil thickness, until it approaches that seen during bulk ion irradiation (i.e. far from the foil surface). Fig. 10 illustrates the expected dependence of microstructure on foil thickness. Because defect motion is thermally activated, the dependence defect density on foil thickness was not observed at low temperatures.

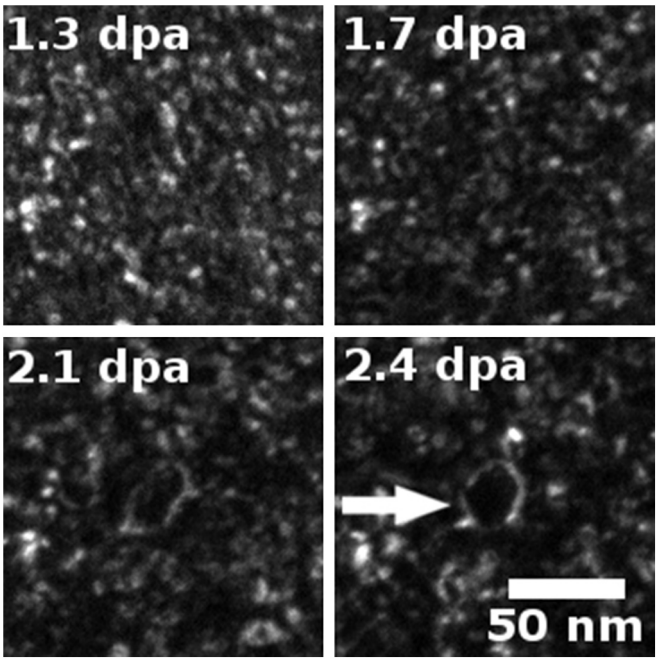

Fig. 5. Several dark-field TEM images with g = 220 (g,3g) captured from the video taken during the irradiation of $ZrC_{0.9}$ between 1.3 and 2.6 dpa showing the formation of a larger dislocation loop by defect coalescence. Images are shown in dose increments of approximately 0.4 dpa, and an arrow at 2.4 dpa indicates the dislocation loop of interest.

3.4. Comparison of $ZrC_{0.8}$ and $ZrC_{0.9}$ irradiated microstructure

Both $ZrC_{0.8}$ and $ZrC_{0.9}$ were irradiated at several temperatures in this work. For example, after irradiation at 473 K, both ZrC compositions showed a high density of black-dot defects, while at 1073 K, both showed a coarse microstructure with loops and tangled dislocation segments. This was true of the microstructures resulting from irradiations at all the temperatures listed in Table 3. We conclude that the irradiated microstructures of $ZrC_{0.8}$ and $ZrC_{0.9}$ are similar over the range of temperatures in this study.

This lack of dependence on ZrC stoichiometry can be understood in a straightforward manner. Because the stoichiometry variation in ZrC is accommodated by vacancies on the carbon sub-lattice [25], it is likely that the carbon sub-lattice does not have a strong influence on the development of radiation damage in ZrC. It can be reasoned that, for $ZrC_{0.8}$ and $ZrC_{0.9}$ with 10% and 20% vacancies on the carbon sub-lattice, one could expect that if the nucleation and growth of defect clusters were controlled by carbon vacancies, the accumulation of defects during irradiation would vary between the two. Additionally, the barriers for carbon and zirconium vacancy migration (4.41 eV and 5.44 eV respectively), as reported by Zheng et al. [22], are quite high and would not activate in the temperature range studied. Furthermore, the antisite defect energy is very high (greater than 11 eV [26]) so that the C and Zr sub-lattices are essentially independent of each other. Finally, with 10% and 20% carbon vacancies, it is difficult for irradiation generated carbon

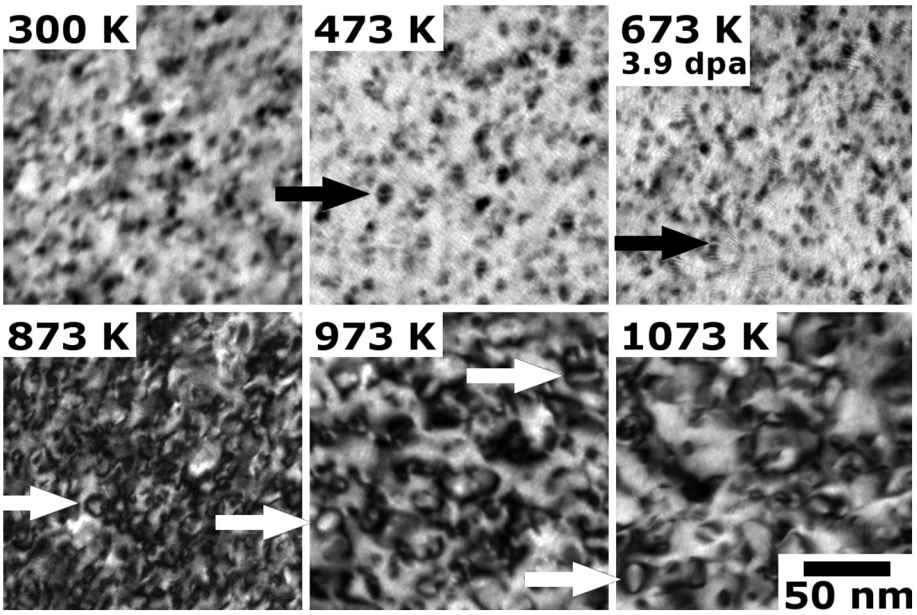

Fig. 6. Bright-field images of the microstructures resulting from irradiating $ZrC_{0.9}$ to 6.4 dpa (except where noted at 673 K) at temperatures ranging from 300 to 1073 K. Dislocation loops with (black) and without (white) double-arc contrast are indicated by the arrows.

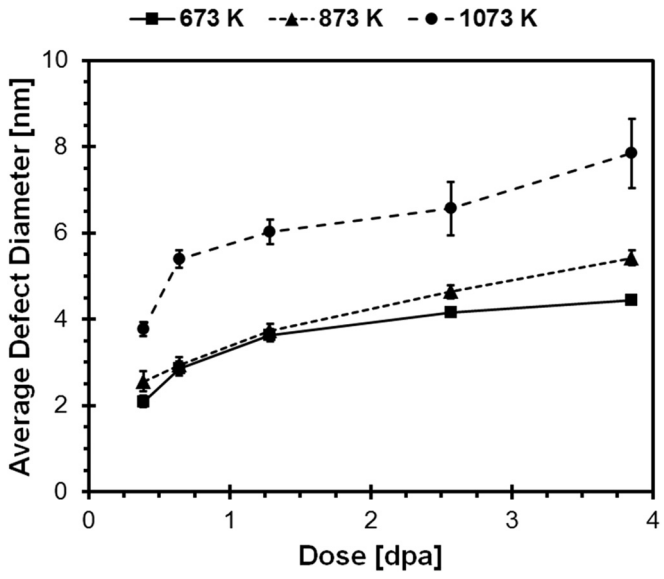

Fig. 7. Measurements of mean defect diameter for $ZrC_{0.9}$ irradiated up to 3.9 dpa at 673, 873 and 1073 K. The error bars show the 95% confidence interval for the average of the defect diameter measurements at each dose point.

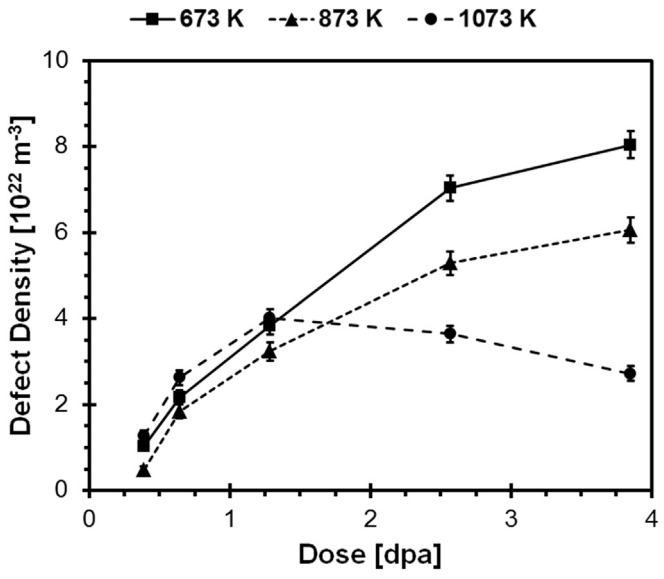

Fig. 8. Measurements of defect density for $ZrC_{0.9}$ irradiated up to 3.9 dpa at 673, 873 and 1073 K. The error bars show the 95% confidence interval associated with the total number of defects counted at each dose point assuming a random spatial distribution of defects.

interstitials to survive recombination. This indicates that the likely defect controlling the microstructure evolution in ZrC is zirconium interstitials and interstitial clusters.

3.5. Diffraction pattern changes during irradiation

As mentioned in subsec:IVEM, diffraction patterns were systematically recorded from the imaged regions at selected doses during irradiation. While the ZrC lattice parameter did not measurably change, extra diffraction rings and spots developed during all irradiations except those completed at 300 K and 473 K. The diffraction rings appeared around 1.3–2.6 dpa and intensified as the dose increased. Fig. 11 shows two examples acquired during irradiations at 50 K and 1073 K. Complete diffraction rings developed at low temperatures and more textured rings or spot patterns developed at higher temperatures (approximately 873 K and up). The d-spacings associated with the low temperature rings and the high temperature textured rings and spots, relative the ZrC lattice parameter, were the same. Fig. 12 shows a bright-field/dark-field pair acquired after irradiating to 12.8 dpa at 50 K; the dark-field image was formed using a portion of the diffraction ring that developed during irradiation. The features observed in the dark-field image appear to be equiaxed and correspond to the larger dark spots observed in the bright-field image.

The diffraction rings and spots that appeared during irradiation were indexed and were consistent with a face-centered cubic (FCC) lattice with a measured lattice parameter of 0.506 nm, or 8% larger

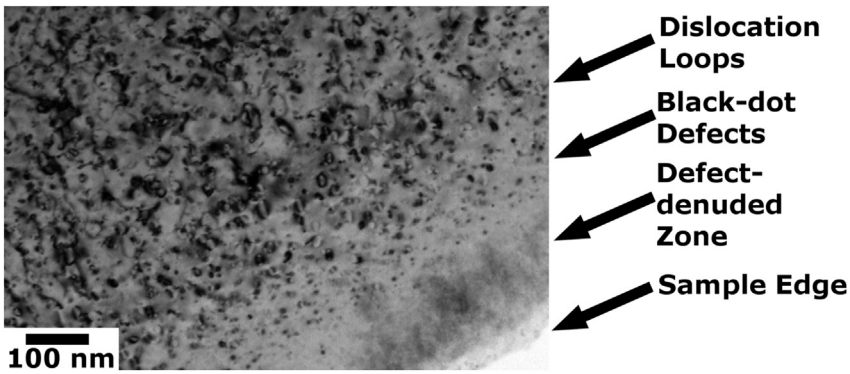

Fig. 9. A bright-field image acquired near the sample edge showing the variation in microstructure with thickness after irradiating $ZrC_{0.9}$ to 5.1 dpa at 1073 K.

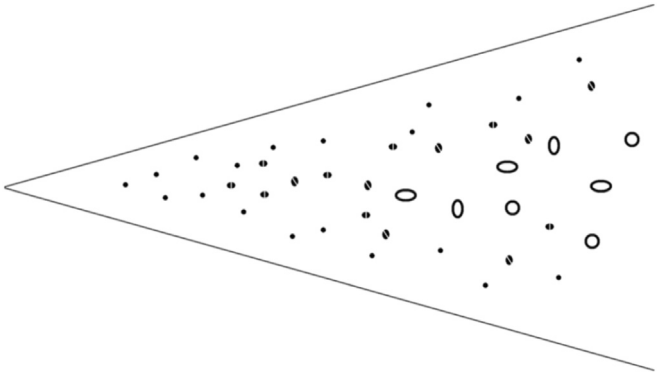

Fig. 10. A cross sectional diagram showing the postulated defect structure resulting from the loss of defects to the surface at temperatures above 873 K.

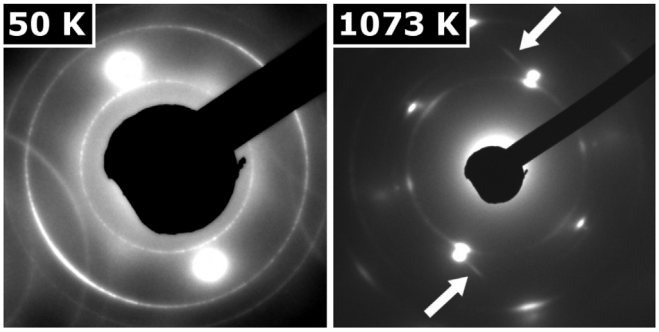

Fig. 11. Diffraction patterns acquired after irradiating $ZrC_{0.9}$ to 12.8 dpa at 50 K and 1073 K. Diffraction rings developed at both temperatures and streaking occurred at 1073 K as indicated by the arrows.

than the ZrC lattice. Depending on the particular diffraction pattern, up to seven diffraction rings were indexed. These observations are similar to those made by Gan et al., who, during *in situ* irradiation at the IVEM, also observed FCC diffraction rings with a lattice parameter 8% larger than ZrC [6]. Additionally, Gosset, et al. observed diffraction rings after bulk ion irradiation of ZrC at room temperature. The authors in that study attributed the rings to a zirconia phase which formed on the surface of samples that had been pre-thinned before irradiation [8].

[3] The cubic phase of zirconia has a lattice parameter of 0.5128 nm (ICDD # 49-1642).

Although the lattice parameter of 0.506 nm is close to that of the zirconia high temperature phase,[3] attributing these diffraction rings to zirconia has a few difficulties as it is not clear how oxidation could occur at 20 K and also because ZrO_2 is monoclinic (or tetragonal) at the temperatures studied. The size of the features observed in dark-field suggests that these could be very small precipitates of a second phase which are severely distorted while maintaining coherency with the substrate.

In addition to the diffraction rings, streaks developed in the diffraction pattern during irradiations at 300 K and above. The streaks appeared to be more intense at higher temperatures, but no systematic diffraction patterns were recorded to directly compare at different temperatures. The streaks appeared between either {111} and {220} reflections or {200} and {111} reflections when the sample was tilted near a ⟨220⟩ zone axis. In both cases, the streaks were in a ⟨111⟩ direction. The streak orientation indicates a relaxation of the diffraction condition in the ⟨111⟩ direction, and could possibly be due to presence of stacking faults associated with Frank loops, such as those observed by Yang et al. using rel-rod dark-field imaging [7].

4. Discussion

The response of ZrC to ion irradiation can be separated into two different regimes. At lower temperatures (approximately 300 K and below), the accumulation of radiation damage in the form of black dot defects is likely controlled by athermal processes leading to the similar damage structures observed over this temperature range. Above these temperatures, however, a dependence of the irradiated

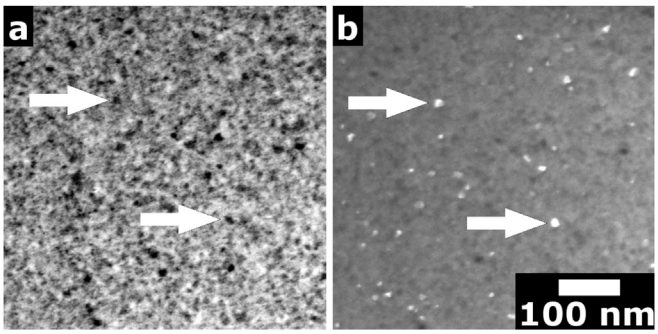

Fig. 12. Bright-field (a) and dark-field (b) micrographs recorded at 12.8 dpa at 50 K showing the same location (corresponding to the left diffraction pattern in Fig. 11). The dark-field image is recorded using a portion of the second diffracted ring from the center. Arrows indicate features that are common between the bright-field and dark-field images.

microstructure on irradiation temperature is observed, whereby high irradiation temperatures result in increased defect diameter and decreased defect density. As the defect cluster diameter increases, individual dislocation loops can be discerned. In this temperature range it is likely that the thermally activated motion of defects has increased to the point that it supersedes the athermal processes occurring at low temperatures.

We can infer the processes involved in the thermally activated defect growth regime. Because calculations of defect migration energies have shown that there are high barriers to migration for both carbon and zirconium vacancies [22], these defects would not be mobile at the temperatures used in these experiments. Since this means that vacancies cannot agglomerate, this explains why no voids were observed in this study as there would be no mechanism for void growth. Calculations indicate that thermally activated mobility of both carbon and zirconium interstitials would be possible within the temperature range of these experiments. However, due to the high concentration of structural carbon vacancies in the sub-stoichiometric ZrC_x compound, carbon interstitials would recombine quickly, and it is difficult to imagine a situation in which they could accumulate and form defect clusters. Therefore, the most likely candidate for the formation and growth of defect clusters is zirconium interstitials.

The results from this experiment agree well with previous *in situ* irradiation experiments at room temperature and 800 °C, during which black dot defects formed at room temperature and dislocation segments were observed after irradiating at 800 °C [6]. Examination after bulk proton irradiations at 800 °C to 0.7 and 1.5 dpa showed that both defect diameter and density increased with dose, matching the present results for that dose range [7]. Bulk proton irradiations performed at 800 °C [10], however, resulted in defect densities that were an order of magnitude lower and defect diameters that were twice as large for $ZrC_{0.9}$ than those found in the present study. A couple of differences between the two experiments may account for the differences in results. These experiments were carried out with a dose rate of 4.7×10^{-5} dpa/s, almost 30 times lower than used in this study when calculated using the same displacement energies for Zr and C. It is possible that the higher dose rate in this study resulted in a saturation of a higher number of smaller defects, because there was relatively less time for defect migration which limited coalescence and growth.

A bulk proton irradiation study of ZrC_x was performed at 1125 °C to 2 dpa by Yang et al. [11] to investigate the effects of sample stoichiometry. The results showed that the dislocation diameters varied little for the sub-stoichiometric material, which agrees well with the observations made in these experiments. However, defect size increased with carbon content in the hyper-stoichiometric material. In addition, it was noted that there was increased loop density near graphite phases. While the weak dependence on carbon content for sub-stoichiometric ZrC_x is verified, it appears that other mechanisms for defect nucleation or growth may occur in the hyper-stoichiometric compound. This may be understood within the presently explained mechanisms in that the structural carbon vacancy concentration is lower in the hyper-stoichiometric compound. It is possible that the carbon vacancy concentration in the hyper-stoichiometric samples is low enough that carbon interstitials are able to contribute to the formation and growth of dislocation loops. Because carbon interstitials are more mobile than zirconium interstitials [22], they are able to increase the growth rate of dislocation loops. Graphite phases may locally act as a source for additional carbon atoms during irradiation which would explain the increased defect density near these phases.

The comparison of the results of this study to those obtained from neutron irradiation are of great importance for the use of ZrC in nuclear reactors. The work performed by Snead et al. [9] included, among other things, TEM defect analysis of $ZrC_{0.87}$ after irradiation in the High Flux Isotope Reactor (HFIR). While these irradiations were performed at temperatures ranging from 635–1480 °C (908–1753 K), it does overlap the highest irradiation temperatures of the present study which had a maximum irradiation temperature of 1073 K. After neutron irradiation, loops were identified as Frank loops at 1023 °C (1296 K), and prismatic loops had formed at 1496 °C (1769 K). These are in agreement with the edge-on loops with {111} and {220} habit planes observed after *in situ* irradiation at 1073 K. Also in agreement with the present study, average loop diameter tended to increase, and loop density tended to decrease, with increased irradiation temperature during neutron irradiation. Additionally, the average defect diameter and defect density after neutron irradiation at 660 °C (933 K), approximately 4 nm and 3×10^{22} m^{-3}, respectively, are similar to those presented in Figs. 7 and 8; a direct comparison of values is not possible because the imaging condition is not clearly stated in Ref. [9].

It would be expected, however, for differences in the microstructure to develop after neutron irradiation vs. *in situ* ion irradiation as a result of, among other things, thin film effects and differences in dose rate. During *in situ* ion irradiation, such as used in this study, a thin foil with thickness on the order of a few hundred nanometers or less is irradiated. With this geometry, there is a large concentration of free surface which can act as a sink for defects and suppress the concentration of freely migrating defect clusters. This could in turn suppress defect nucleation and growth resulting in lower visible defect density and smaller visible defects. The thin film effect was clearly observed during these experiments (see Fig. 9), where a defect-denuded zone developed in the thinnest regions of the sample.

The dose rate during these *in situ* ion irradiations, 1.6×10^{-3} dpa/s, is several orders of magnitude greater than during neutron irradiation. It is thought that changes to one irradiation variable can be accommodated by changes to another variable such that the desired irradiation feature remains unchanged [27]. Specifically, a higher dose rate can be accommodated by irradiating at a higher temperature, or conducting an irradiation at increased dose rate is equivalent to holding the dose rate constant but decreasing the irradiation temperature. Because of the observed trends of loops with temperature, it would be expected that irradiating at a higher dose rate in ZrC would result in smaller average loop diameter and higher loop density.

5. Conclusion

In situ ion irradiation using the Intermediate Voltage Electron Microscope (IVEM) at Argonne National Laboratory was used to study the microstructure evolution of ZrC_x under irradiation. Irradiations were carried out using 1 MeV Kr ions up to doses of 12.8 dpa, or 5×10^{19} ions/m^2, at temperatures ranging from 20 to 1073 K. The detailed conclusions are as follows:

1. During low temperature irradiation (at 300 K and below), damage was observed in the form of small defect clusters, or “black-dot” damage. The damage appeared after a threshold dose and increased gradually with dose until saturation after several dpa. Once visible defects were created, they were stable and neither moved nor were destroyed during the remainder of the experiment.
2. In the high temperature regime (at 873 K and above), although visible defects did not appear to migrate thermally, interaction of closely spaced defects was observed which resulted in microstructure coarsening through defect coalescence.
3. In the high temperature regime, the foil surface was found to act as a strong sink for defects as demonstrated by the defect-

denuded zone and evolution of defect diameter with foil thickness near the sample edge.
4. No void formation or amorphization were observed at any of the temperatures studied.
5. The irradiated microstructure of ZrC_x was not observed to vary significantly with composition in the range of $x = 0.8–0.9$.
6. Diffraction rings formed during all irradiations except at 300 K and 473 K and were more highly oriented, or textured, at higher temperatures. The ring pattern was indexed and was consistent with an FCC lattice with a lattice parameter 8% larger than that of ZrC.
7. Up to the doses studied, the irradiated microstructure of ZrC appears to be reasonably stable with gradual changes up to 4–6 dpa where it approached saturation. Irradiations to higher doses will be necessary to further explore the stability of ZrC with respect to irradiation.
8. Zirconium interstitials and interstitial clusters are likely dominant in the formation and growth of visible defect clusters in sub-stoichiometric ZrC.

Acknowledgments

This work was funded by the U.S. Department of Energy's Nuclear Engineering University Program project number 10-679. The electron microscopy with *in situ* ion irradiation was accomplished at Argonne National Laboratory at the IVEM-Tandem Facility, a U.S. Department of Energy Facility funded by the DOE Office of Nuclear Energy, operated under Contract No. DE-AC02-06CH11357 by UChicago Argonne, LLC. We thank Pete Baldo and Ed Ryan of Argonne National Laboratory for their invaluable assistance in carrying out the irradiations. We also thank Ming-Jie Zheng, Izabela Szlufarska, Dane Morgan and Yina Huang for their insights and discussions.

References

[1] GIF-002-00, Generation IV International Forum and U.S, DOE NERAC, 2002.
[2] R. Morris, D. Petti, D. Powers, B. Boyack, NUREG-6844, U.S. Nuclear Regulatory Commission, 2004.
[3] D.T. Goodin, J. Am. Ceram. Soc. 65 (1982) 238–242, http://dx.doi.org/10.1111/j.1151-2916.1982.tb10425.x.
[4] K. Minato, T. Ogawa, S. Kashimura, K. Fukuda, M. Shimizu, Y. Tayama, I. Takahashi, J. Nucl. Mater. 172 (1990) 184–196, http://dx.doi.org/10.1016/0022-3115(90)90437-R.
[5] P. Wagner, LA-6984, Los Alamos Scientific Laboratory, 1977. http://dx.doi.org/10.2172/5361609.
[6] J. Gan, M.K. Meyer, R.C. Birtcher, T.R. Allen, J. ASTM Int. 3 (2006) 1–7, http://dx.doi.org/10.1520/JAI12376.
[7] Y. Yang, C.A. Dickerson, H. Swoboda, B. Miller, T.R. Allen, J. Nucl. Mater. 378 (2008) 341–348, http://dx.doi.org/10.1016/j.jnucmat.2008.06.042.
[8] D. Gosset, M. Dollé, D. Simeone, G. Baldinozzi, L. Thomé, J. Nucl. Mater. 373 (2008) 123–129, http://dx.doi.org/10.1016/j.jnucmat.2007.05.034.
[9] L.L. Snead, Y. Katoh, S. Kondo, J. Nucl. Mater. 399 (2010) 200–207, http://dx.doi.org/10.1016/j.jnucmat.2010.01.020.
[10] Y. Huang, B. Maier, T. Allen, Nucl. Eng. Des. 277 (2014) 55–63, http://dx.doi.org/10.1016/j.nucengdes.2014.06.001.
[11] Y. Yang, W.Y. Lo, C. Dickerson, T.R. Allen, J. Nucl. Mater. 454 (2014) 130–135, http://dx.doi.org/10.1016/j.jnucmat.2014.07.071.
[12] W. Mackie, C. Hinrichs, J. Cryst. Growth 87 (1988) 101–106, http://dx.doi.org/10.1016/0022-0248(88)90347-8.
[13] C. W. Allen, L. L. Funk, E. A. Ryan, in: MRS Proceedings, vol. 396, Cambridge Univ Press, pp. 641. http://dx.doi.org/10.1557/PROC-396-641.
[14] J.F. Ziegler, M. Ziegler, J. Biersack, Nuclear instruments and methods in physics research section B: beam interactions with materials and atoms 268 (2010) 1818–1823, http://dx.doi.org/10.1016/j.nimb.2010.02.091.
[15] R.E. Stoller, M.B. Toloczko, G.S. Was, A.G. Certain, S. Dwaraknath, F.A. Garner, Nuclear instruments and methods in physics research section B: beam interactions with materials and atoms 310 (2013) 75–80, http://dx.doi.org/10.1016/j.nimb.2013.05.008.
[16] C.A. Schneider, W.S. Rasband, K.W. Eliceiri, Nat. Methods 9 (2012) 671–675, http://dx.doi.org/10.1038/nmeth.2089.
[17] D.B. Williams, C.B. Carter, Transmission Electron Microscopy, Springer, 2009, http://dx.doi.org/10.1007/978-0-387-76501-3_1.
[18] E. Prince, International Tables for Crystallography, in: Mathematical, Physical and Chemical Tables Third Edition, vol. C, Wiley, Hoboken, 2004.
[19] P. Kelly, A. Jostsons, R. Blake, J. Napier, Phys. Status Solidi A 31 (1975) 771–780, http://dx.doi.org/10.1002/pssa.2210310251.
[20] C. Topbasi, A.T. Motta, M.A. Kirk, J. Nucl. Mater. 425 (2012) 48–53, http://dx.doi.org/10.1016/j.jnucmat.2011.08.046.
[21] A.T. Motta, J. Nucl. Mater. 244 (1997) 227–250, http://dx.doi.org/10.1016/S0022-3115(96)00740-4.
[22] M.J. Zheng, I. Szlufarska, D. Morgan, J. Nucl. Mater. 457 (2015) 343–351, http://dx.doi.org/10.1016/j.jnucmat.2014.11.059.
[23] M. Li, M. Kirk, P. Baldo, D. Xu, B. Wirth, Philos. Mag. 92 (2012) 2048–2078, http://dx.doi.org/10.1080/14786435.2012.662601.
[24] A. Motta, D. Olander, Acta Metall. Mater. 38 (1990) 2175–2185, http://dx.doi.org/10.1016/0956-7151(90)90085-U.
[25] H.W. Hugosson, U. Jansson, B. Johansson, O. Eriksson, Chem. Phys. Lett. 333 (2001) 444–450, http://dx.doi.org/10.1016/S0009-2614(00)01414-7.
[26] S. Kim, I. Szlufarska, D. Morgan, J. Appl. Phys. 107 (2010) 053521, http://dx.doi.org/10.1063/1.3309765.
[27] L. Mansur, J. Nucl. Mater. 216 (1994) 97–123. http://dx.doi.org/10.1016/0022-3115(94)90009-4.
[28] M.J. Zheng, D. Morgan, I. Szlufarska, Ab initio study on the threshold displacement energy in zirconium carbide, J. Nucl. Mater. (2015). Accepted for publication.